

# The distribution function of dark matter in massive haloes

Radosław Wojtak,<sup>1</sup> Ewa L. Lokas,<sup>1</sup> Gary A. Mamon,<sup>2,3</sup> Stefan Gottlöber,<sup>4</sup>  
Anatoly Klypin<sup>5</sup> and Yehuda Hoffman<sup>6</sup>

<sup>1</sup>*Nicolaus Copernicus Astronomical Center, Bartycka 18, 00-716 Warsaw, Poland*

<sup>2</sup>*Institut d'Astrophysique de Paris (UMR 7095: CNRS and Université Pierre & Marie Curie), 98 bis Bd Arago, F-75014 Paris, France*

<sup>3</sup>*GEPI (UMR 8111: CNRS and Université Denis Diderot), Observatoire de Paris, F-92195 Meudon, France*

<sup>4</sup>*Astrophysikalisches Institut Potsdam, An der Sternwarte 16, 14482 Potsdam, Germany*

<sup>5</sup>*Department of Astronomy, New Mexico State University, Box 30001, Department 4500, Las Cruces, NM 88003, USA*

<sup>6</sup>*Racah Institute of Physics, Hebrew University, Jerusalem 91904, Israel*

1 November 2021

## ABSTRACT

We study the distribution function (DF) of dark matter particles in haloes of mass range  $10^{14}$ – $10^{15}M_{\odot}$ . In the numerical part of this work we measure the DF for a sample of relaxed haloes formed in the simulation of a standard  $\Lambda$ CDM model. The DF is expressed as a function of energy  $E$  and the absolute value of the angular momentum  $L$ , a form suitable for comparison with theoretical models. By proper scaling we obtain the results that do not depend on the virial mass of the haloes. We demonstrate that the DF can be separated into energy and angular momentum components and propose a phenomenological model of the DF in the form  $f_E(E)[1 + L^2/(2L_0^2)]^{-\beta_{\infty} + \beta_0} L^{-2\beta_0}$ . This formulation involves three parameters describing the anisotropy profile in terms of its asymptotic values ( $\beta_0$  and  $\beta_{\infty}$ ) and the scale of transition between them ( $L_0$ ). The energy part  $f_E(E)$  is obtained via inversion of the integral for spatial density. We provide a straightforward numerical scheme for this procedure as well as a simple analytical approximation for a typical halo formed in the simulation. The DF model is extensively compared with the simulations: using the model parameters obtained from fitting the anisotropy profile, we recover the DF from the simulation as well as the profiles of the dispersion and kurtosis of radial and tangential velocities. Finally, we show that our DF model reproduces the power-law behaviour of phase space density  $Q = \rho(r)/\sigma^3(r)$ .

**Key words:** galaxies: clusters: general – galaxies: kinematics and dynamics – cosmology: dark matter

## 1 INTRODUCTION

The distribution function (DF) provides the most general and complete way of statistical description of dark matter (DM) haloes. It carries maximum information on the spatial and velocity distributions of particles in such objects. Our knowledge on the DF is still being improved, mostly due to numerical experiments. In the last few years cosmological simulations have revealed increasingly detailed features of phase-space structure of DM haloes. These numerical results provide useful constraints on theoretical models of the DF. One property of interest in this field is the anisotropy of the velocity dispersion tensor. It has been demonstrated that the outer parts of the haloes exhibit more radially anisotropic trajectories than the halo centre (see e.g. Colín, Klypin & Kravtsov 2000; Fukushige & Makino 2001; Wojtak et al.

2005; Mamon & Lokas 2005; Cuesta et al. 2007). This feature, besides the well-studied density profile, has been considered as the main point of reference in the attempts at construction of a reliable model of the DF.

So far, a few approaches to this problem have been proposed. Cuddeford (1991) generalized the Osipkov-Merritt model (Osipkov 1979; Merritt 1985) to the DF which generates an arbitrary anisotropy in the halo centre and becomes fully radial at infinity. Although an analytical inversion for these models exists, the anisotropy profile cannot be reconciled with the numerical results: the rise from central to outer anisotropy is too sharp and the outer orbits are too radial (see Mamon & Lokas 2005). An & Evans (2006a) noticed that a non-trivial profile of the anisotropy can be obtained from a sum of DFs with a constant anisotropy for which an analytical inversion is known (Cuddeford 1991;

Kochanek 1996; Wilkinson & Evans 1999). However, the resulting anisotropy profiles are decreasing functions of radius and do not agree with those measured in cosmological simulations. Recently a very elegant method has been presented by Baes & van Hese (2007). The authors introduced a general ansatz for the anisotropy profile and then, for a given potential-density pair, derived the DF as a series of some special functions. This approach works well under the condition that the potential can be expressed as an elementary function of the corresponding density. This requirement, however, is not satisfied by many models, including the NFW density profile (Navarro, Frenk & White 1997) which is commonly used as a good approximation of the universal density profile of DM haloes.

The DF inferred from the simulation gives a possibility to test directly the analytical models. According to the Jeans theorem any spherically symmetric system in the state of equilibrium should possess a DF which is a function only of energy and the absolute value of angular momentum. This theoretical postulate was taken into account in the computation carried out by Voglis (1994) and Natarajan, Hjorth & van Kampen (1997). In the first case the DF was obtained for a single relaxed halo which formed from cosmologically consistent initial conditions. It was shown that there were two main contributions to the DF, the halo population and the core population of particles. Both were effectively described by two independent phenomenological fits. Natarajan et al. (1997) determined the DF for a sample of cluster-size haloes formed in cosmological simulations. Their selection of objects included those with substructures and departing from equilibrium. They also discussed and took into account in their calculation the effect of boundary conditions defined by the virial sphere. However, the final results were not used to test quantitatively any model of the DF.

It seems that two main approaches to study the DF, namely theoretical modelling and feedback from the simulations, evolved rather separately barely crossing each other. The rare exceptions include the work of Lokas & Mamon (2001) who used the Eddington formula to derive numerically the DF following from the NFW profile in the isotropic case and that of Widrow (2000) who considered more general cuspy profiles and Osipkov-Merritt anisotropy. This paper is devoted to combining both approaches and providing a coherent analysis of the DF from the viewpoints of the simulations as well as the model construction. Our main aim is to propose a phenomenological model of the DF that recovers the results from the simulations as accurately as possible.

Our effort is mainly motivated by the future applications of the derived DF to the dynamical modelling of galaxy clusters. Although subhaloes in general have different density and velocity distributions than DM particles (Diemand, Moore & Stadel 2004), massive subhaloes (those likely to host galaxies) are distributed like DM particles (Faltenbacher & Diemand 2006). Although the correspondence between the massive subhaloes and galaxies in real clusters remains to be proven, our results should at least in principle be applicable to kinematic data sets for galaxy clusters. The traditional approach to do such modelling was to reproduce the velocity dispersion profile of the galaxies by solving the Jeans equation (see e.g. Katgert, Biviano & Mazure 2004). It is well known however that from the dispersion alone one cannot constrain all the interesting parameters (such

as the virial mass, the concentration of the NFW profile and anisotropy) because of the density-anisotropy degeneracy. One can break this degeneracy by using the fourth order velocity moment, the kurtosis, and solving an additional higher-order Jeans equation (Lokas 2002; Lokas & Mamon 2003; Lokas et al. 2006; Wojtak & Lokas 2007). Although this approach has many advantages (e.g. it does not require the knowledge of the full DF), it has been applied till now only for constant-anisotropy models and the calculation of velocity moments requires the binning of the data in which some information is lost. Since the number of galaxies with measured redshifts per cluster is still rather low (of the order of a few hundred for the best-studied, nearby clusters) it is essential that all the available information is used. This can be obtained by fitting the projected DF to the data directly.

A few approaches along these lines have been attempted already. For example, Mahdavi & Geller (2004) used a simple DF of the form  $f(E, L) \propto E^{\alpha-1/2} L^{-2\beta}$  (which yields constant anisotropy) to constrain the mass profile and orbital structure using combined kinematic data sets for nearby galaxy groups and clusters, while van der Marel et al. (2000) in their study of CNOC clusters did not assume an explicit form for the energy-dependent part of the DF, but still used the constant anisotropy. Wojtak et al. (2007) used a simplified form of the projected isotropic DF constructed from the projected density combined with a Gaussian distribution for the line-of-sight velocities to study the properties of members versus interlopers in simulated kinematic data sets. None of the DFs used so far, however, reflects accurately the true properties of cluster-size DM haloes found in  $N$ -body simulations.

The paper is organized as follows. Section 2 provides the theoretical framework and defines all the basic quantities used later on in the paper. In the next section we discuss the details of the computation of the DF of DM particles in the haloes formed from cosmological simulations and provide examples of the results. Section 4 is devoted to the derivation of a phenomenological model of the DF; we discuss the separability of the DF in energy and angular momentum and present an explicit formula for the  $L$ -dependent part of DF. An extensive comparison of the model with the simulations is presented in Section 5, where we also provide an analytical approximation for the energy-dependent part of the DF obtained for an average halo. Finally, the discussion follows in Section 6.

## 2 THEORETICAL FRAMEWORK

This section summarizes the theoretical background of the paper. First, we introduce scaling properties consistent with the NFW density profile. We will use this profile in the paper, but our approach is not restricted to this particular density distribution and can be easily generalized to any profile consistent with simulations (see below). Second, we briefly describe the relation between the differential DF and the DF itself. Finally, we discuss the consequences of the finite volume of the virialized area of a halo. In particular, the relation between the DF and its differential form is properly modified to account for this effect.

## 2.1 Scaling properties

It is a well known fact that the density profiles of DM haloes formed in cosmological simulations exhibit striking similarity. NFW showed that most of them are well fitted within the virial sphere by the universal two-parameter profile which can be expressed in the following way

$$\rho_{\text{NFW}}(x) = \frac{1}{4\pi(\ln 2 - 1/2)} \frac{M_s}{r_s^3} \frac{1}{x(1+x)^2}, \quad (1)$$

where  $x = r/r_s$ . The two free parameters are the scale radius  $r_s$  and the mass enclosed within the sphere of this radius  $M_s$ . The (positive) gravitational potential inferred from the Poisson equation reads (Cole & Lacey 1996; see also Lokas & Mamon 2001)

$$\Psi_{\text{NFW}}(r) = V_s^2 \frac{\ln(1+x)}{x}, \quad (2)$$

where the velocity unit  $V_s$  is related to the circular velocity  $V_{\text{cir}}(r_s)$  at the scale radius via  $V_s = V_{\text{cir}}(r_s)(\ln 2 - 1/2)^{-1/2}$ .

Let us note that  $r_s$ ,  $V_s$  and  $M_s$  define a set of natural units of the NFW model. By scaling any quantity by a proper combination of them we remove the explicit dependence on the free parameters of the NFW model. This is an essential property if we want to study the dynamics of a whole class of haloes with NFW-like density profiles. Hereafter, we will keep this scaling in all equations in the text. In many places we will also use a unit of the angular momentum  $L_s$  as a substitute for  $V_s r_s$ .

## 2.2 The distribution function

The DF is a fundamental concept in statistical mechanics of  $N$ -body systems. It describes the phase-space density of particles of such a system without any detailed knowledge of the time evolution of  $N$  trajectories. Following the Jeans theorem, a steady-state DF, which is of interest for us here, depends on the phase-space coordinates only through the integrals of motion. Although the shape of DM haloes is in general better approximated by a three-axial ellipsoid rather than a sphere (see e.g. Gottlöber & Yepes 2007), it is still very effective to assume spherical symmetry in dynamical approach. Given that the streaming motions and internal rotation within the virial sphere are negligible compared to higher velocity moments, spherical symmetry implies that the DF can be expressed as

$$f(\mathbf{r}, \mathbf{v}) = f(E, L), \quad (3)$$

where  $E$  is the positively defined binding energy and  $L$  the absolute value of the angular momentum per unit mass

$$E = \Psi(r) - \frac{1}{2} \mathbf{v}^2 \quad (4)$$

$$\mathbf{L} = \mathbf{r} \times \mathbf{v}. \quad (5)$$

The gravitational potential in equation (4) is related to the DF through the Poisson equation

$$\nabla^2 \Psi(\mathbf{r}) = -4\pi G \int f(\mathbf{r}, \mathbf{v}) d^3 \mathbf{v}. \quad (6)$$

The most natural and straightforward probe of  $f(E, L)$  in numerical experiments is the so-called differential DF defined in the following way

$$N(E, L) = \frac{d^2 M}{dE dL}. \quad (7)$$

One may intuitively interpret this function as mass density in energy-angular momentum space. The DF itself can be simply derived dividing  $N(E, L)$  by the volume  $g(E, L)$  of the hypersurface of constant energy and angular momentum embedded in the phase space

$$f(E, L) = \frac{N(E, L)}{g(E, L)}. \quad (8)$$

It is easy to show that the volume of this hypersurface reads (see Appendix A)

$$g(E, L) = 8\pi^2 L T_r(E, L), \quad (9)$$

where  $T_r(E, L)$  is the radial period of an orbit given by the following integral over radius from the pericentre to the apocentre

$$T_r = 2 \int_{r_p}^{r_a} \frac{dr}{\sqrt{2[\Psi(r) - E - L^2/(2r^2)]}}. \quad (10)$$

The upper panel of Fig. 1 shows a contour map of  $g(E, L)$  (dotted lines) calculated for the NFW gravitational potential (2). The  $L_{\text{max}}(E)$  line is the profile of maximum angular momentum which consists of points corresponding to circular orbits. This curve divides the energy-angular momentum plane into an area describing the physical orbits of a system (below  $L_{\text{max}}$ ) and the zone not permitted by mechanics (above  $L_{\text{max}}$ ). Note that we are using the scaling relations introduced in the previous subsection so the results do not depend explicitly on the halo mass  $M_s$  and the scale radius  $r_s$ . In some places later on we will refer to the inverse function for  $L_{\text{max}}(E)$  by  $E_{\text{max}}(L)$ .

Voglis (1994) and Natarajan et al. (1997) showed that the dependence of  $T_r(E, L)$  on the angular momentum is very weak and could be neglected without loss of precision. This is understandable if we note that the NFW-like potentials are still not so far away from the isochrone potential  $\Psi(r) \propto (b + \sqrt{b^2 + r^2})^{-1}$  which leads to purely energy-dependent  $T_r$  proportional to  $E^{-3/2}$  (Binney & Tremaine 1987). Following Natarajan et al. (1997) we will use this feature to simplify expression (9). To do this we first note that the volume of the hypersurface of constant energy  $g_E$  is given by

$$g_E(E) = \int_0^{L_{\text{max}}(E)} g(E, L) dL. \quad (11)$$

Taking advantage of the weak dependence of  $T_r$  on  $L$ , equation (10), we get

$$g(E, L) \approx 2 \frac{g_E(E) L}{L_{\text{max}}^2(E)}. \quad (12)$$

On the other hand, one can show that  $g_E(E)$  reads (see Appendix A)

$$g_E(E) = 16\pi^2 \int_0^{r_{\text{max}}(E)} \sqrt{2(\Psi(r) - E)} r^2 dr, \quad (13)$$

where  $r_{\text{max}}(E)$  is the apocentre radius of the radial orbit. Inserting (13) into (12) one immediately gets a very simple approximation for  $g(E, L)$  involving only a one-dimensional integral without singularities, in contrast with  $g(E, L)$  derived by expression (10). We find that this approximation reproduces the exact formula (9) with enough accuracy. Taking

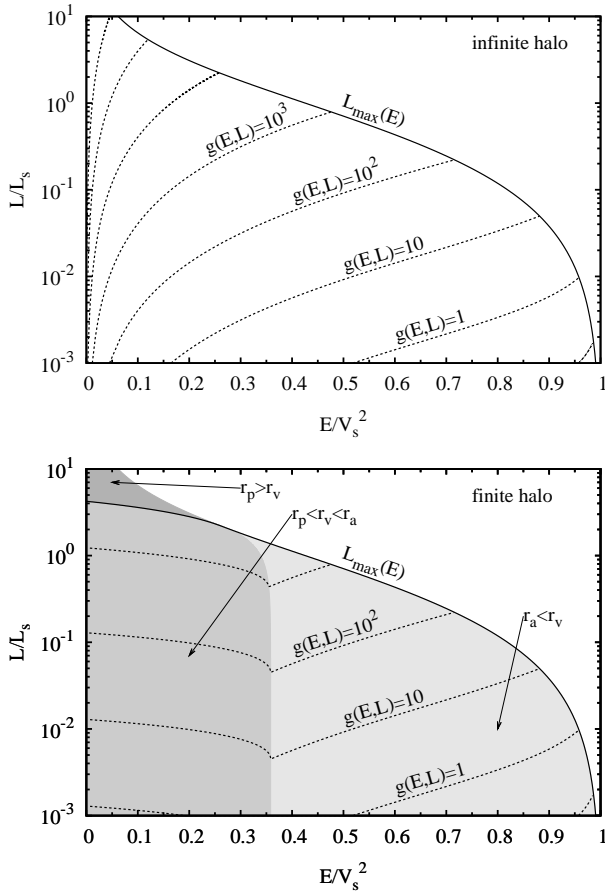


**Figure 1.** The volume of the hypersurface of constant energy and angular momentum for the infinite halo (upper panel) and the finite halo limited by the virial sphere of radius  $r_v = 5 r_s$  (lower panel). In both cases the NFW profile was assumed. Solid lines show the profiles of the maximum angular momentum of a given system. In the lower panel the three shades of gray mark the three characteristic zones according to the orbit size defined by the relation of the virial radius  $r_v$  to the pericentre radius  $r_p$  and the apocentre radius  $r_a$ , as labelled.

advantage of its numerical simplicity we use it in majority of our calculations.

### 2.3 Boundaries of the haloes

So far we have discussed the relation between the DF and its differential form for an infinite system. In practice, however, we restrict our numerical analysis to the interior of the virial sphere which separates the equilibrium part of a halo from the infall region. We define the virial radius  $r_v$  of this sphere by

$$M_v = \frac{4}{3} \pi r_v^3 \Delta_c \rho_c, \quad (14)$$

where  $M_v$  is the virial mass,  $\rho_c$  is the present critical density and  $\Delta_c$  is the virial overdensity. Another parameter commonly used to describe the size of the virial sphere in terms of  $r_s$  is the concentration  $c = r_v/r_s$ .

The existence of the boundary of the virialized part of the halo implies that  $T_r$  given by (10) must be replaced by

$$T_r = 2 \int_{r_p}^{\min\{r_a, r_v\}} \frac{dr}{\sqrt{2[\Psi(r) - E - L^2/(2r^2)]}}, \quad (15)$$

where the upper limit of the integral is a minimum of the virial radius and the radius at the apocentre (see Appendix A for details). Combining (15) with (9) one gets a general formula for the volume  $g(E, L)$  in the presence of a spherical boundary of a halo. Contrary to the conclusion of Natarajan et al. (1997), we find that the approximation (12) is no longer justified for orbits extending beyond the virial sphere ( $r_a > r_v$ ). This follows from the fact that angular momentum dependence of (15) becomes non-negligible and the integral (11) cannot be simplified to the form of (12).

Using (9) and (15) with the NFW potential, we calculated  $g(E, L)$  for a halo limited by the virial sphere of radius  $r_v = 5 r_s$  (see the lower panel of Fig. 1). As expected, the result differs from an infinite system by the orbits with  $r_a > r_v$  and remains unchanged for trajectories wholly included within the virial sphere.

## 3 THE DISTRIBUTION FUNCTION FROM THE SIMULATION

### 3.1 The simulation

For our  $N$ -body simulation we have assumed the WMAP3 cosmology (Spergel et al. 2007) with matter density  $\Omega_m = 0.24$ , the cosmological constant  $\Omega_\Lambda = 0.76$ , the dimensionless Hubble parameter  $h = 0.73$ , the spectral index of primordial density perturbations  $n = 0.96$  and the normalization of power spectrum  $\sigma_8 = 0.76$ . We have used a box of size  $160 h^{-1} \text{Mpc}$  and  $1024^3$  particles. Thus the particle mass was  $3.5 \times 10^8 M_\odot$ . Starting at redshift  $z = 30$  we followed the evolution using the MPI version of the Adaptive Refinement Tree (ART) code (Kravtsov, Klypin & Khokhlov 1997).

We identified clusters with the hierarchical friends-of-friends (FOF) algorithm (Klypin et al. 1999) with a linking length of 0.17 times the mean inter-particle distance which roughly corresponds to an overdensity of 330. We have selected 36 clusters at redshift  $z = 0$  in the range of virial mass  $(0.15\text{--}2) \times 10^{15} M_\odot$ , where the virial overdensity parameter appropriate for our cosmological model was assumed  $\Delta_c = 93.8$  (Lokas & Hoffman 2001). Our sample did not include clusters with two substructures of approximately the same mass and a poor fit of the NFW profile suggestive of a recent major merger.

Starting from the FOF position of the cluster we have determined the highest density peak as the final centre of the clusters. This centre coincides with the position of the most massive substructure found at the linking length 8 times shorter and also with the position of the halo found by the BDM halo finder (Klypin et al. 1999).

### 3.2 Computation of the distribution function

In the first step of the computation we calculate the binding energy (4) and the angular momentum (5) per unit mass for each particle within the virial sphere of each halo. Spherical symmetry implies that we have to apply in (4) the radial profile of the gravitational potential

$$\Psi(r) = \int_r^\infty \frac{GM(r)dr}{r^2}, \quad (16)$$

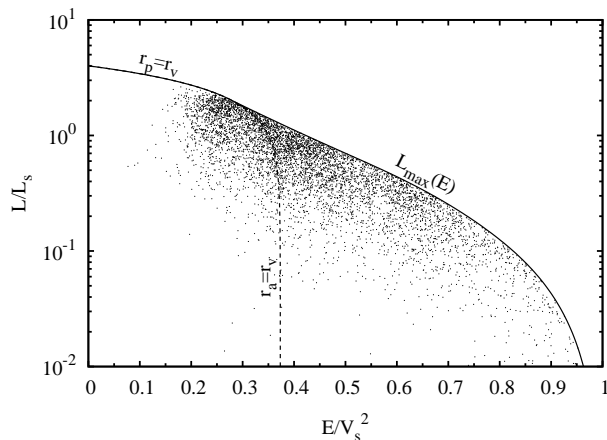


**Figure 2.** Energies and angular momenta of particles within the virial sphere of one of the simulated haloes. Solid and dashed lines mark the profile of the maximum angular momentum and the limit of vanishing radial velocity at  $r_v$  respectively. To make the picture less obscure we plotted only 1 percent of the particles.

where  $\Psi(\infty) = 0$ . However, the mass profile of the equilibrium part of a halo reaches no further than the virial radius. On the other hand, all analytical models of the DF involve the density profile extending to infinity. We found that the only coherent way to reconcile both facts is to split the integral (16) in two parts

$$\Psi(r) = \int_r^{r_v} \frac{GM(r)dr}{r^2} + \int_{r_v}^{\infty} \frac{GM_{\text{NFW}}(r)dr}{r^2}. \quad (17)$$

The first term is evaluated numerically by integration of a discrete mass profile. The second term is an analytical extension with the NFW density profile which is an assumption of the DF model introduced in the following section. Its contribution to the potential is a constant equal to  $V_s^2 \ln(1+c)/c$ .

Fig. 2 shows the resulting energies and angular momenta of particles inside the virial sphere of one of the simulated haloes. The profile of the maximum angular momentum (solid line) and the profile of vanishing radial velocity at the virial sphere (dashed line) were calculated for the exact gravitational potential given by (17). All particles occupy the area permitted by mechanics or lie very close to the boundary line. Interestingly, quite a large fraction of them have orbits extending beyond the virial sphere. As noted in the previous section, we keep  $V_s^2$  and  $L_s$  as units of energy and angular momentum respectively. The parameters of the NFW model were obtained for each halo by fitting the NFW formula to the density profile measured in logarithmic radial bins.

In the next step we determine for each halo the differential DF given by (8). In this calculation we used our own version of the FiEstAS (Field Estimator for Arbitrary Spaces) algorithm designed to infer the density field from a scatter diagram embedded in a space of any number of dimensions (see Ascasibar & Binney 2005 for more details). As a result of this computation we get an estimate of  $N(E, L)$  at all points of the energy-angular momentum plane corresponding to the particles inside the virial sphere. Once  $N(E, L)$  is calculated the DF can be easily obtained via (8). As discussed in section 2, we used approximation (12) for the orbits contained inside the virial sphere and the exact

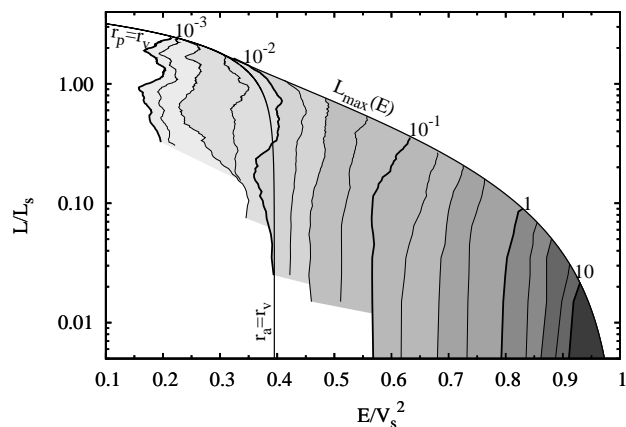
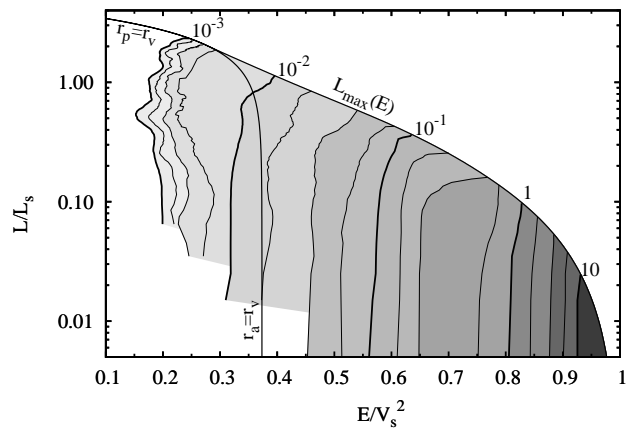


**Figure 3.** Contour maps of the DF of DM particles inside the virial sphere of two example haloes. The profile of the maximum angular momentum is indicated by  $L_{\text{max}}(E)$  and the line of vanishing radial velocity at the virial sphere by  $r_a = r_v$  (apocentre at the virial sphere) or  $r_p = r_v$  (pericentre at the virial sphere).

formula (9) with (15) for trajectories extending beyond  $r_v$ . We found that the additional advantage of expression (12) is that it could be evaluated at any point of the energy-angular momentum plane. This helps us to keep the estimates of the DF obtained for points with angular momentum lying slightly above  $L_{\text{max}}(E)$ .

In order to derive a contour map or a profile of the DF we introduce a regular dense mesh on the energy-angular momentum plane and find the median value of the DF in each cell. Such a set of median points is considered as the final numerical approximation of the DF and is used in preparation of all plots in this paper. Fig. 3 shows two examples of the resulting contour maps obtained for two different haloes. The unit of the DF in this and following Figures is  $M_s/r_s^3/V_s^3$ . The interval between the iso-DF lines is fixed at value 0.25 of the logarithmic scale. The lack of the DF estimation in the lower part of each diagram arises from the fact that this zone is occupied by very few particles (see e.g. Fig. 2) so that no information on the distribution can be retrieved. Let us note that this is an effect of the finite mass resolution.

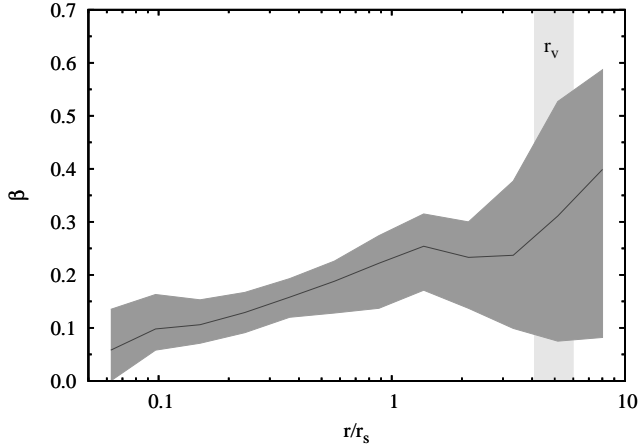


**Figure 4.** The profile of the anisotropy parameter. The solid line and the dark gray area are the median and the interquartile range of the profiles obtained for individual haloes and rescaled by  $r_s$  inferred from fitting the NFW profile.

#### 4 THE ANALYTICAL MODEL OF THE DISTRIBUTION FUNCTION

A general form of the DF for spherical systems in the state of equilibrium is a function of energy and the absolute value of angular momentum  $f(E, L)$ . In our approach we assume that the DF is separable in energy and angular momentum

$$f(E, L) = f_E(E)f_L(L). \quad (18)$$

This is the first assumption that considerably narrows the family of possible solutions. Therefore, it is necessary to check how robust it is. We address this problem in the next section, where we present an extensive comparison of the analytical model with the simulations.

The angular momentum part of the DF in equation (18) specifies the anisotropy of velocity dispersion tensor. This quantity is commonly described with the so-called anisotropy parameter

$$\beta(r) = 1 - \frac{\sigma_\theta^2(r)}{\sigma_r^2(r)}, \quad (19)$$

where  $\sigma_r$  and  $\sigma_\theta$  are the radial and the tangential velocity dispersions respectively and we assume there are no streaming motions. The values of this parameter range from  $-\infty$  for circular orbits to 1 for purely radial trajectories. Fig. 4 shows the average anisotropy profile of the simulated haloes used for the measurement of the DF. The light gray rectangle in the background of the plot indicates the position of the virial radius. It is clearly seen that the anisotropy is typically a growing function of radius, with values  $\sim 0.07$  in the halo centre and  $\sim 0.3$  at the virial sphere (see e.g. Mamon & Lokas 2005 and Cuesta et al. 2007 for comparison). On the other hand, the considerable width of the interquartile range of the measured  $\beta(r)$  (dark gray region) signifies that the profiles of single haloes differ among each other. Occasionally flat or decreasing profiles are measured. It seems that a simple and general enough analytical model of the anisotropy should possess at least three free parameters which determine asymptotic values of  $\beta(r)$  for small and large radii and a scale of transition between them. We proceed with the construction of such a model by introducing a proper ansatz for  $f_L(L)$ .

Louis (1993) showed that the following asymptotes of the angular momentum part of the DF

$$f_L(L) \propto \begin{cases} 1 & \text{for } L \ll L_0 \\ L^{-2\beta_\infty} & \text{for } L \gg L_0, \end{cases} \quad (20)$$

where  $L_0$  is an angular momentum constant, lead to constant anisotropy  $\beta_\infty$  at infinity ( $r^2\Psi(r) \gg L_0^2$ ) and  $\beta = 0$  in the halo centre. This result can be easily generalized to the case of a non-isotropic velocity distribution in both limits of radius. First, let us note that the central part of the halo is dominated by the particles with small angular momenta, namely  $L^2 \leq 2r^2\Psi(r) \ll L_0^2$ . Then, remembering that the DF of constant anisotropy takes the form (Hénon 1973; Binney & Tremaine 1987; Lokas 2002)

$$f(E, L) = f_E(E)L^{-2\beta}, \quad (21)$$

it is easy to notice that the formula (20) can be rewritten in the following way

$$f_L(L) \propto \begin{cases} L^{-2\beta_0} & \text{for } L \ll L_0 \\ L^{-2\beta_\infty} & \text{for } L \gg L_0, \end{cases} \quad (22)$$

where  $\beta_0$  is the central anisotropy of a system. As shown by An & Evans (2006b), the upper limit for  $\beta_0$  is equal to  $\gamma/2$ , where  $r^{-\gamma}$  is the density profile near the halo centre. This means that for the NFW density model we have  $\beta_0 \leq 1/2$ .

The simplest function obeying the asymptotic conditions formulated above is a double power-law function

$$f_L(L) = \left(1 + \frac{L^2}{2L_0^2}\right)^{-\beta_\infty + \beta_0} L^{-2\beta_0}. \quad (23)$$

As shown in the following section, this ansatz leads to a very realistic anisotropy profile that fits well the  $\beta(r)$  profiles of simulated haloes. Furthermore, the simplicity of formula (23) guarantees that the energy part of the DF can be quite easily calculated via the inversion of the integral equation

$$\rho(r) = \iiint f_E(E) \left(1 + \frac{L^2}{2L_0^2}\right)^{-\beta_\infty + \beta_0} L^{-2\beta_0} d^3v. \quad (24)$$

The key idea of this procedure lies in an analytical simplification of the right-hand side of (24) to a one-dimensional integral. The resulting equation is then solved numerically for  $f_E(E)$ . The technical details of this calculation are summarized in Appendix B. Once the full form of the DF is determined one can also calculate the velocity moments. All formulae are reduced to one-dimensional integrals which can be easily evaluated numerically (see Appendix C).

The top row of Fig. 5 shows the anisotropy, dispersion  $\sigma_r$  and kurtosis  $\kappa_r = \langle v_r^4 \rangle / \sigma_r^4$  of the radial velocity inferred from the model of the DF. The calculations were carried out assuming the NFW density profile and four sets of model parameters chosen to illustrate the flexibility of the model:  $\beta_0 = 0.1$  and  $\beta_\infty = 0.3, 0.5$  (solid and dashed lines respectively);  $\beta_0 = \beta_\infty = 0.3$  (dotted line);  $\beta_0 = 0.4$  and  $\beta_\infty = 0.1$  (dashed-dotted line). In all cases the transition value of  $L_0 = 0.25 L_s$  was used.

The dispersion profiles for the two models with increasing  $\beta(r)$ , as expected, differ only for large radii which is the effect of different values of  $\beta_\infty$ . Interestingly, the corresponding kurtosis profiles clearly signify flat-topped velocity distribution in the outer part of the halo ( $\kappa_r < 3$ ), highly peaked distribution in the centre ( $\kappa_r > 3$ ) and roughly Gaussian for radii around  $r_s$  ( $\kappa_r \approx 3$ ). On the other hand, non-increasing

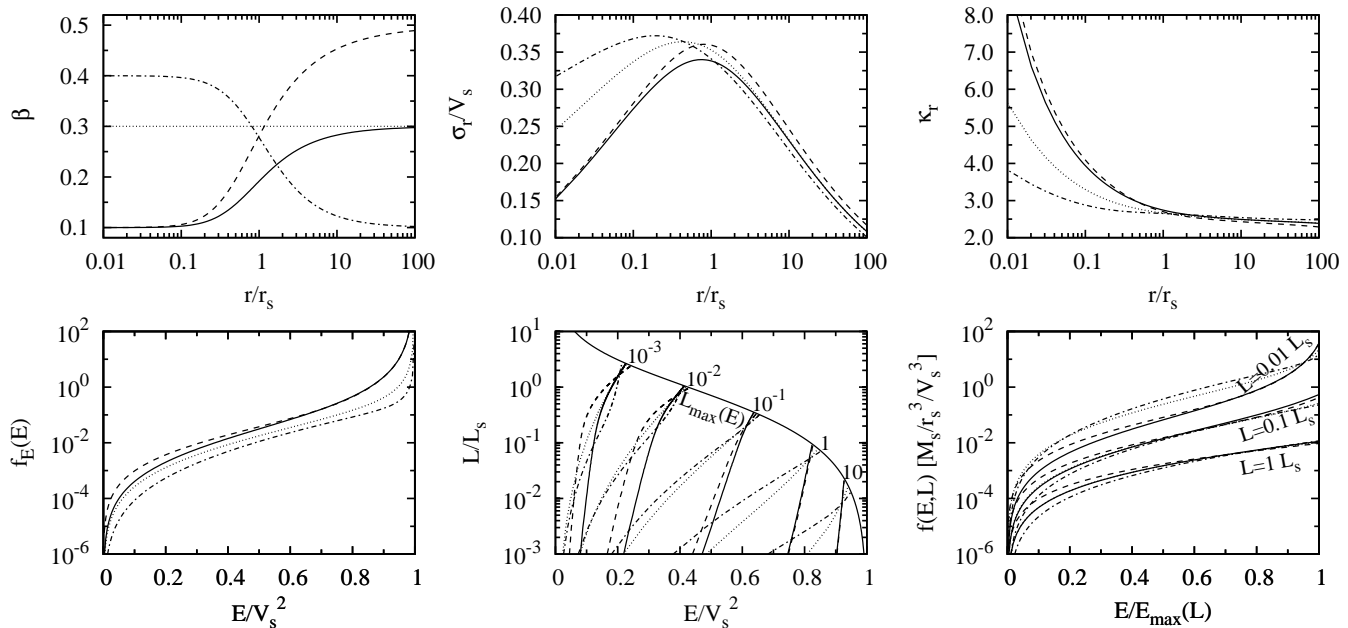


**Figure 5.** The top panels show (from left to right) the anisotropy, dispersion and kurtosis of the radial velocity inferred from the model of the DF with four sets of parameters:  $\beta_0 = 0.1$ ,  $L_0 = 0.25 L_s$  and  $\beta_\infty = 0.3, 0.5$  (solid and dashed lines respectively);  $\beta_0 = \beta_\infty = 0.3$ ,  $L_0 = 0.25 L_s$  (dotted line);  $\beta_0 = 0.4$ ,  $L_0 = 0.25 L_s$  and  $\beta_\infty = 0.1$  (dashed-dotted line). The corresponding DFs for the same sets of parameters are plotted in the bottom panels in terms of: the energy part of the DF  $f_E(E)$  (left), iso-DF lines with values indicated along the curve of maximum angular momentum (middle) and the profiles of the DF for three values of angular momentum (right). In all calculations the NFW density profile was assumed.

$\beta(r)$  profiles lead to less peaked velocity distributions in the centre. It seems therefore that the typical anisotropy of DM haloes, as shown in Fig. 4, is expected to coincide with the kurtosis rapidly growing towards the halo centre (see also Fig. 10 below). As we will see in the following section, this is one of the most characteristic features of the phase-space structure of massive DM haloes.

In the bottom panels of Fig. 5 we plotted the DFs corresponding to four sets of model parameters, as described above. The three panels from the left to the right show the energy part of the DF, contour maps and the profiles for three fixed values of angular momentum. The plots reveal some interesting signatures of the specific shape of  $\beta(r)$  profile. For example, the inclination of the iso-DF lines with respect to the energy axis decreases with increasing  $\beta_0$ : more isotropic  $\beta$  at the centre corresponds to more vertical iso-DF lines; also the shape of the lines is somewhat different. These features are also to some extent visible in the contour maps of the DF for two simulated haloes in Fig. 3. The upper map represents a halo with an increasing  $\beta(r)$ , whereas the second one depicts the case of a decreasing  $\beta(r)$  profile. Both haloes are analyzed in terms of velocity moments and the DF in the following section.

Recently Mamon & Lokas (2005) found that the simulation data are well reproduced by the anisotropy profile of the form

$$\beta(r) = \frac{1}{2} \frac{r}{r + r_{1/4}}, \quad (25)$$

where  $r_{1/4}$  is the radius where  $\beta = 0.25$ . Assuming  $\beta_0 = 0$  and  $\beta_\infty = 0.5$  in our DF model, we made a comparison of the resulting anisotropy with the functional form (25).

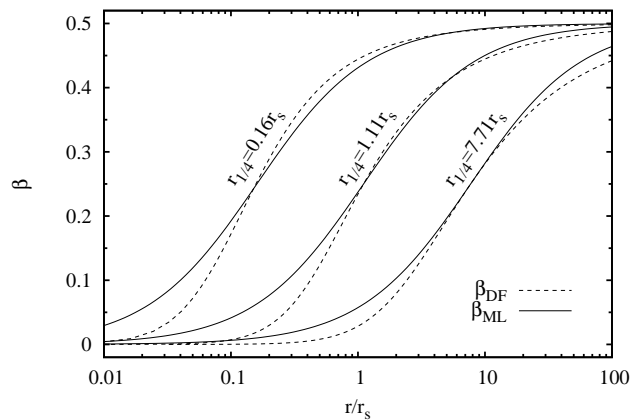


**Figure 6.** Comparison between the functional form of the anisotropy (25) proposed by Mamon & Lokas (2005) ( $\beta_{ML}$ ) and  $\beta(r)$  inferred from the DF model ( $\beta_{DF}$ ) with  $\beta_0 = 0$  and  $\beta_\infty = 0.5$ .

Fig. 6 shows both anisotropies for three values of  $r_{1/4}$ . Note that both  $\beta(r)$  profiles have similar shapes, although our anisotropy profile has a somewhat sharper rise at small radii.

We also find that the radius  $r_0$  characteristic of the DF model, for which  $\beta$  is the mean of the limiting values

$$\beta(r_0) = \frac{\beta_0 + \beta_\infty}{2}, \quad (26)$$

depends weakly on  $\beta_0$  and  $\beta_\infty$ . For parameter ranges leading to  $\beta(r)$  profiles covering the interquartile area of anisotropy from the simulation ( $0 < \beta_0 < 0.15$ ,  $0 < \beta_\infty < 0.6$  and

$0.04 < L_0/L_s < 25$ ), this radius is well (within 5 percent accuracy) approximated by

$$r_0/r_s = 3.69(L_0/L_s)^{0.97} + 2.27(L_0/L_s)^{1.9}. \quad (27)$$

## 5 COMPARISON WITH THE SIMULATION

### 5.1 The distribution function

The DF proposed in the previous section is a phenomenological model in the sense that it possesses free parameters whose values should be adjusted to the simulation data. All three parameters were introduced to determine a family of anisotropy profiles so that it is  $\beta(r)$  that is most sensitive to the variations of  $\beta_0$ ,  $\beta_\infty$  and  $L_0$ . Consequently, we decided to constrain the parameters of the model by fitting the  $\beta(r)$  profile inferred from the DF model to the median profile measured in simulated DM haloes. The best-fitting parameters are:  $\beta_0 = 0.09$ ,  $\beta_\infty = 0.34$  and  $L_0 = 0.198 L_s$ . The corresponding best-fitting profile of the anisotropy is plotted as a dashed line in the lower left panel of Fig. 9.

Once the model parameters are adjusted the DF can be compared with its counterpart measured from the simulation. Fig. 7 shows this comparison in terms of a contour map and the profiles for constant angular momentum or energy. Dark gray regions in all panels indicate the interquartile range of the DF values within the halo sample. The lighter gray area in the background of the upper diagram marks the points of vanishing radial velocity at the virial radius  $r_v$ . Its boundaries are fixed by the first and third quartile of virial radii in the halo sample,  $4.1r_s$  and  $6.0r_s$  respectively.

Although some deviations of the model (dashed lines) from the results of the simulations are visible, in general the theoretical profiles are included within the interquartile range or lie very close to its boundaries. As expected, the strongest discrepancy between the model and the simulation is present in the part of the energy-angular momentum plane populated by the particles with orbits extending beyond the virial sphere (the area to the left of the  $r_a = r_v$  line). However, given that this is the only part of the energy-angular momentum plane affected by the infalling material, we think that the observed differences are acceptable.

### 5.2 The separability of the distribution function

A critical point of the derivation of the DF presented in the previous section was the factorization introduced by equation (18). In order to inspect the robustness of this assumption we propose a simple test. We calculate the ratio of the DF from the simulation to the energy part of the DF model with parameters adjusted to the anisotropy profile from the simulation. Under the assumption that the real DF is factorizable in energy and angular momentum, we can expect that the resulting ratio should be a weak function of energy equal to  $f_L(L)$  given by (23). Fig. 8 shows that the variations of this ratio with respect to  $f_L(L)$  are of the same order as the width of the interquartile range which means that separability is acceptable from the statistical point of view. A small systematic deviation can be seen for  $L \sim 0.1 L_s$ . However, this is certainly a local feature since this trend is not repeated in other profiles. Let us emphasize that this test of separability depends strongly on the reliability of  $f_L(L)$ .

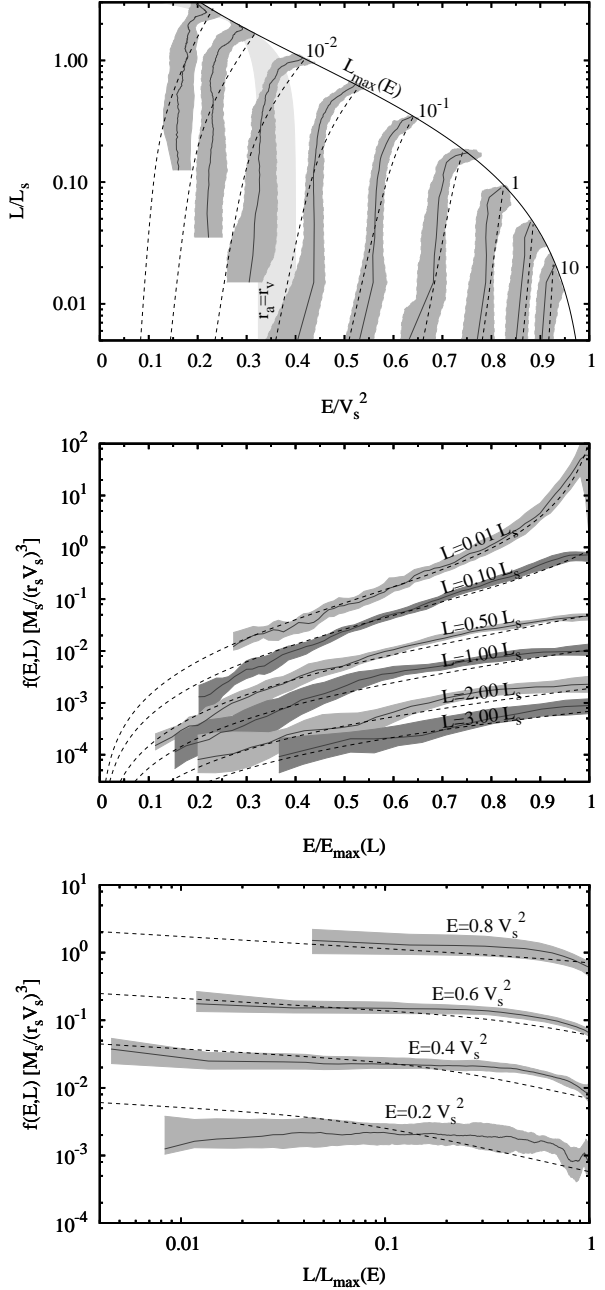


**Figure 7.** Comparison between the DF measured for DM particles inside the virial sphere of the simulated haloes and the model with parameters adjusted to the median anisotropy,  $\beta_0 = 0.09$ ,  $\beta_\infty = 0.34$  and  $L_0 = 0.198 L_s$ . Solid lines and gray areas stand for median profiles and interquartile ranges of the DF measured in the halo sample, whereas the dashed lines correspond to the model. The light gray area in the background of the upper diagram indicates the points of vanishing radial velocity at the virial radius  $r_v$ . Its boundaries are fixed by the first and third quartile of virial radii in the halo sample.

One can imagine that an incorrect form of  $f_L(L)$  would likely lead to a negative result of the test, whether  $f(E, L)$  is separable or not. On the contrary, a positive result of such a test in our case means that not only is the assumption of factorization valid but the approximation for  $f_L(L)$  is reasonable as well.

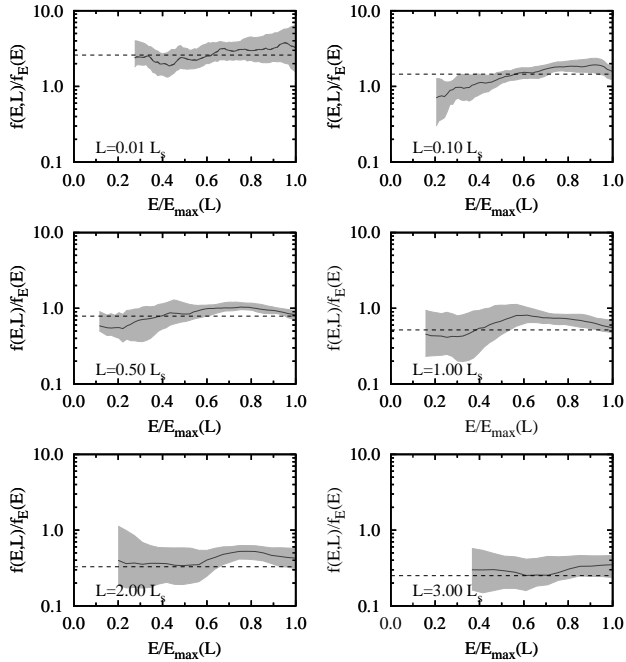


**Figure 8.** The ratio of the DF inferred from the 36 simulated haloes to the energy part of the DF model with parameters adjusted to the median anisotropy profile. Each panel shows the profile for the constant value of angular momentum indicated in the lower left corner. Solid lines and gray areas represent the median profiles and interquartile ranges respectively. The dashed lines indicate the values of  $f_L(L)$  given by the ansatz (23).

### 5.3 Velocity moments

Further comparison between the simulation and the DF model can be done in terms of velocity moments. This is depicted in Fig. 9 where the dispersion and kurtosis of the radial and tangential velocity are plotted. In the bottom part of this figure we show the profiles of the anisotropy  $\beta(r)$  and  $\beta_4$  parameter which measures the anisotropy of a tensor of the fourth velocity moment. By analogy with the parameter  $\beta(r)$  we defined  $\beta_4(r)$  in the following way

$$\beta_4(r) = 1 - \frac{\langle v_\theta^4 \rangle(r)}{\langle v_r^4 \rangle(r)}. \quad (28)$$

The dashed lines in each panel of Fig. 9 are the model predictions, except for the  $\beta(r)$  profile (lower left panel) which is a fit of the model providing constraints on parameter values given in the previous subsection. Theoretical dispersion profiles coincide very well with the profiles from the simulation. We notice quite a good agreement also for the  $\beta_4(r)$  parameter. On the other hand, theoretical profiles of the kurtosis are systematically biased towards higher values, but typically by less than 10 percent. Nevertheless, their shapes clearly recover the shapes of the median profiles from the simulation. Moreover, for both the radial and tangential velocity a characteristic growth of  $\kappa$  from value  $\lesssim 3$  around the virial radius up to  $\gtrsim 4$  in the halo centre, is seen.

Although the kurtosis bias is enclosed within acceptable limits (kurtosis is known to be sensitive to any noise), it would be desirable to find out the reason for this behaviour. Since our statistical samples consist of  $10^4 - 10^5$  particles per radial bin, we ruled out a possibility of a bias of the

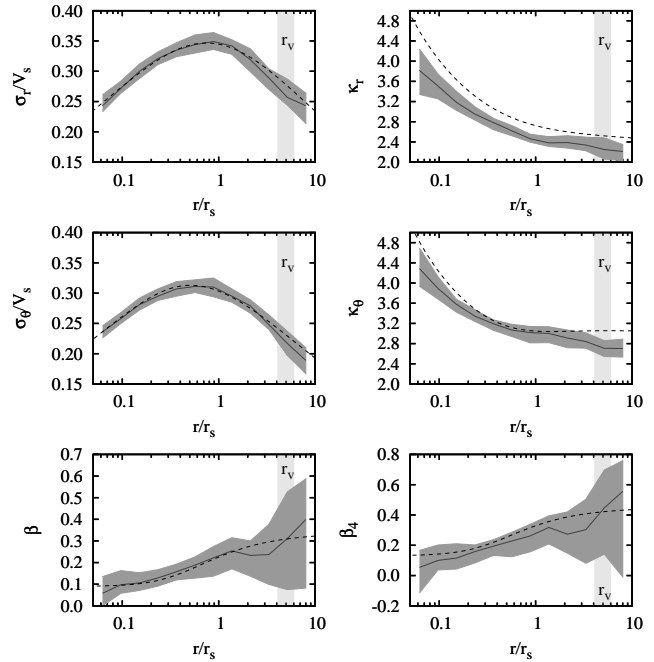


**Figure 9.** Velocity moments of the radial and tangential velocity (top and middle panels) and the anisotropy of the dispersion tensor  $\beta(r)$  and the fourth velocity moment tensor  $\beta_4(r)$  defined by (28). The solid line and the dark gray area are the median and the interquartile range of the profiles obtained for individual haloes and rescaled by  $r_s$  and  $V_s$  inferred from fitting the NFW profile. Dashed lines are the profiles inferred from the DF model with parameters adjusted to the median anisotropy measured from the simulation. In the case of anisotropy  $\beta(r)$  (lower left panel) this line shows the fit of the model.

kurtosis estimator (see Lokas & Mamon 2003). We also excluded the possibility that this is caused by some specific assumptions of the model. For example, changing the NFW density distribution to the 3D Sersic profile, which fits the simulation data even better (Navarro et al. 2004; Merritt et al. 2005; Prada et al. 2006), we still encounter the same bias. In addition, perturbing the model parameters of  $f_L(L)$  does not explain the situation either.

We therefore conclude that the slight discrepancy in the predictions of our model concerning the kurtosis must signify reaching the limitations of the theoretical approach based on using the global, smooth gravitational potential of a system. We suppose that the problem is caused by the presence of substructures which perturb locally the trajectories of particles with respect to the orbits determined by the global potential of a halo. What one gets from the simulation is really a convolution of the velocity distribution expected from the model involving a global potential with the distribution of velocity perturbations occurring due to density fluctuations. The estimation of the importance of this effect is a complicated task since the perturbation of the particle orbit depends on many variables, such as the distribution of substructures, softening of the potential and particle velocity. However, some qualitative conclusions can be drawn. First, note that low-velocity particles are affected by the density perturbations more strongly. Consequently, the peak of the resulting velocity distribution is suppressed and the tails are preserved which may effectively decrease

the kurtosis (see Fig. 9). Second, the effect of the perturbation on the velocity dispersion is a higher order correction compared to the dispersion obtained for a system with a global potential. This means that the resulting dispersion profiles are barely changed and they are still expected to coincide well with theoretical predictions.

It seems an intriguing issue that the profile of tangential kurtosis signifies Gaussianity of the velocity distribution at radii around  $r_s$  where the logarithmic slope of the density profile is equal to  $-2$ . One could suppose that some signatures of the so-called isothermal sphere are locally present. Interestingly, this statement is also supported by the shape of the DF for  $E \leq \Psi(r_s) \approx 0.7 V_s^2$  that is the energy range of particles at  $r_s$ . Referring to the middle panel of Fig. 7 it is easy to notice that the DF grows exponentially with energy, as expected for systems not very different from the isothermal sphere. The distribution of the radial velocity, on the other hand, takes the Gaussian form for radii around  $0.3 r_s$ . This difference could be a consequence of the non-vanishing anisotropy parameter, which is not accounted for in the classical formulation of the isothermal model (Binney 1982; Binney & Tremaine 1987).

So far we tested the DF model for a typical halo associated with the median properties of our halo sample. In order to check the applicability of our model more extensively we repeat such comparison for single haloes. The DF in this case is expected to differ from one halo to another due to the observed variety of anisotropy profiles. Results of this analysis are summarized in Fig. 10. To save space we included only five haloes with representative, rather different anisotropy profiles (upper panels), from the most strongly increasing profile in the left panel to a decreasing one on the right-hand side. The second and fifth panels correspond to the haloes for which contour maps of the DF are shown in Fig. 3 (the top and bottom panel respectively). We restricted the number of profiles to those most essential: we plot the dispersion and kurtosis of the radial velocity and the anisotropies  $\beta(r)$  and  $\beta_4(r)$ . We also show the profiles of the DF for three values of angular momentum or energy. In all panels the solid lines represent simulation results, whereas dashed lines are the predictions of the model. As in Fig. 9, dashed lines in the case of parameter  $\beta(r)$  indicate best fitting profiles of the model. Gray regions in the panels of two bottom rows mark the interquartile ranges of the DF which describe the scatter of points resulting from the FiEstAS algorithm.

From the analysis of Fig. 10 we conclude that all profiles, regardless of the anisotropy, are very well reproduced by our model of the DF. In general, the theoretical DF does not exceed the limits of the interquartile range or lies very close to its boundaries (see two bottom rows of panels in Fig. 10). Surprisingly, we find that the agreement is usually almost equally good when the model is applied to the haloes with massive substructures which were rejected from our sample. This is certainly good news for the future applications of our DF to the dynamical modelling of galaxy clusters which very often display signatures of recent major mergers.

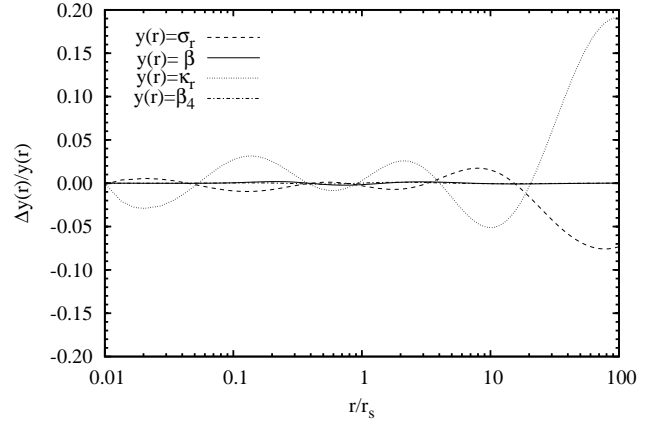


**Figure 11.** Relative errors of velocity moments and anisotropies inferred from the DF obtained with the analytical approximation of  $f_E(E)$  given by (29). All profiles were compared with the results of exact calculations summarized in Appendix C.

| parameter  | $\beta_0 = 0.09$<br>$\beta_\infty = 0.34$ | $\beta_0 = 0$<br>$\beta_\infty = 0.5$ |
|------------|---|---------------------------------------|
| $C$        | 0.000738                                  | 0.001663                              |
| $E_0$      | 0.12903                                   | 0.14124                               |
| $E_1$      | 0.078                                     | 0.07                                  |
| $\alpha_1$ | 2.10                                      | 1.74                                  |
| $E_2$      | 0.071                                     | 0.085                                 |
| $\alpha_2$ | 2.47                                      | 3.01                                  |

**Table 1.** Values of the parameters used in the approximation of the energy part of the DF (29). The first column lists the parameters. The second column gives the parameter values for the model fitted to the anisotropy for the average halo from the simulation ( $\beta_0 = 0.09$  and  $\beta_\infty = 0.34$ ) and the third one gives the values which reproduce the DF for the anisotropy profile (25) ( $\beta_0 = 0$  and  $\beta_\infty = 0.5$ ). In both cases  $L_0 = 0.198 L_s$  was assumed.

#### 5.4 Analytical approximation of the distribution function

The DF discussed in the first subsection is typical in a sense that it describes the statistical macrostate of DM particles in a typical massive halo. With future applications in mind we decided to provide an analytical approximation for the energy part  $f_E(E)$  of this DF which could be used as a substitute for a rather complicated procedure described in Appendix B. We found that the following expression reproduces the numerical DF with good accuracy

$$f_E(E) = C \exp\left(\frac{E}{E_0}\right) E^{\alpha_1/[1+\exp(E/E_1)]} \times (1-E)^{-\alpha_2/[1+\exp\{(1-E)/E_2\}]}, \quad (29)$$

where the values of the parameters are listed in the middle column of Table 1. For completeness we recall that the angular momentum part of the DF is given by (23) with  $\beta_0 = 0.09$ ,  $\beta_\infty = 0.34$  and  $L_0 = 0.198 L_s$ . We have verified that the errors of the dispersion, kurtosis and both anisotropies, when using this approximate formula in the integrals for velocity moments, do not exceed 5 percent within the radial range  $(0.01 r_s, 30 r_s)$  (see Fig. 11). Note that the general form of expression (29) can be effectively used to ap-

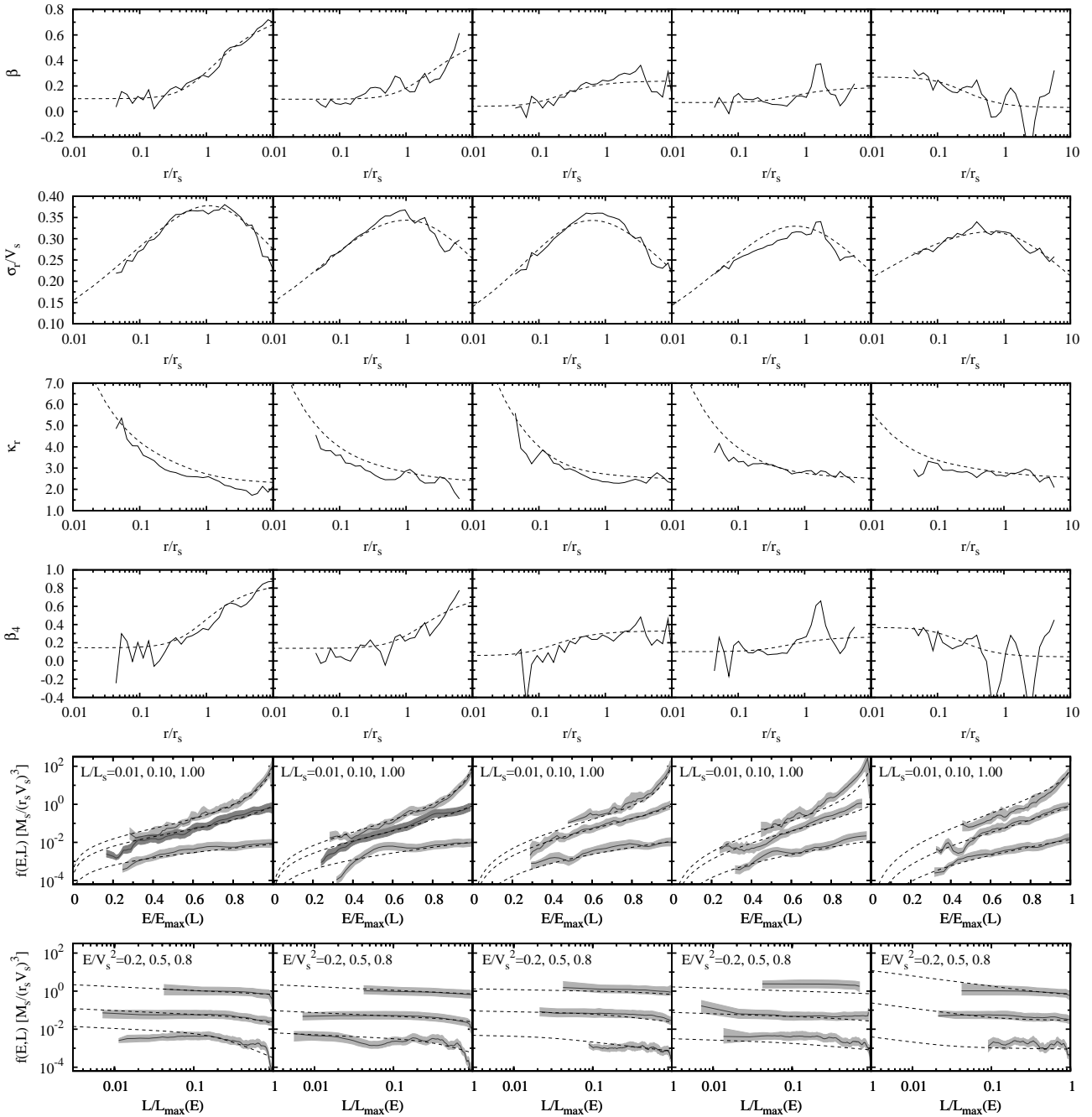


**Figure 10.** Comparison between the model of the DF and the simulation for 5 haloes (in columns) in terms of the anisotropies  $\beta(r)$  and  $\beta_4(r)$ , the dispersion and kurtosis of the radial velocity and the profiles of the DF for different values of angular momentum or energy. Solid and dashed lines show respectively the results from the simulation and the predictions of the model with parameters adjusted to the anisotropy profile. Gray areas and lines in the panels of two bottom rows indicate the interquartile ranges and the medians of the DF for three fixed values of angular momentum or energy given in the upper left corner of each panel (with lower profiles corresponding to higher angular momentum or lower energy).

proximate the DF model also for other sets of parameters. As a second example we include in the third column of the Table also the parameters of a model with  $\beta_0 = 0$ ,  $\beta_\infty = 0.5$  and  $L_0 = 0.198 L_s$  which mimics the anisotropy profile (25) with  $r_{1/4} = 0.9 r_s$ .

## 6 DISCUSSION

We have studied the DF of DM particles inside the virial spheres of the haloes of mass  $10^{14}$ – $10^{15} M_\odot$  formed in the standard  $\Lambda$ CDM cosmological  $N$ -body simulation. In the first part of the paper we presented results of the calculation of the DF from the simulation in the form most suitable for comparison with theoretical models. Then we pro-

posed a phenomenological model of the DF. The model in its part dependent on angular momentum involves three free parameters which specify the anisotropy profile, namely its asymptotic values and the scale of transition between them. We demonstrated that this parametrization is sufficient to reproduce accurately the simulation results in terms of velocity moments as well as the DF itself. The only discrepant point we encountered was a small but statistically significant bias of the theoretical kurtosis with respect to its profiles measured from the simulation. This is probably caused by the presence of substructures perturbing the trajectories of low-velocity particles.

In section 5 we showed that the velocity distribution of a typical halo changes from a flat-topped distribution ( $\kappa < 3$ ) in the outer part to a peaked one ( $\kappa > 3$ ) near the centre. This behaviour was noticed and discussed by others before (e.g. Kazantzidis, Magorrian & Moore 2004; Wojtak et al. 2005). The analysis of the DF presented here suggests that this property of the velocity distribution is correlated with the profile of the anisotropy increasing with  $r$ :  $\beta(r)$  profiles growing faster with  $r$  imply more rapid growth of the kurtosis towards the centre.

As demonstrated by Taylor & Navarro (2001), the profile of the phase-space density  $Q(r) = \rho(r)/\sigma(r)^3$  in DM haloes is well fitted by a power-law function. It seems that the status of this relation is as well established as the NFW fit of the density profile. We checked that  $Q(r)$  profiles inferred from the DF model with parameters adjusted to the median anisotropy (see section 5) coincide well with the corresponding power-law functions (see Fig. 12). In this comparison we assumed the logarithmic slopes of  $-1.92$  (in the case of the dispersion of the radial velocity) and  $-1.84$  (in the case of the total dispersion), the values obtained from the simulations by Dehnen & McLaughlin (2005). The relative residuals of both  $Q(r)$  profiles are of the same order as the scatter of points from the simulations in fig. 1 of Dehnen & McLaughlin (2005). Note that this happens when the DF model is tuned to the mean trend of the  $\beta(r)$  parameter. Therefore one could suspect that both relations, the mean profile of the anisotropy and  $Q(r) \propto r^{-\gamma}$ , are two aspects of some deeper relation. A more general parametrization of the DF might provide some insights towards a more fundamental understanding of this phenomenon.

Although the whole analysis presented in this paper was done in the framework of the NFW density profile, the equations for the numerical inversion (B12) were derived for an arbitrary density distribution. Using this general form one can immediately obtain a family of DFs with our general anisotropy profiles for any potential-density pair. For the commonly used density profiles it is easy to introduce the phase space units analogous to  $r_s$ ,  $V_s$  and  $M_s$  in our case. This reduces the role of the parameters of the density profile to scaling properties so that the final DF model would not explicitly depend on them.

Given our very general parametrization of the  $\beta(r)$  profile, our DF model is expected to provide some impact on the solution of the classical problem of mass-anisotropy degeneracy for spherical systems. In order to obtain more reliable estimates of mass profiles, one could assume the anisotropy profile from the simulation and keep the density profile as the only degree of freedom of the DF. One could then apply the maximum likelihood approach of projected DF, as de-

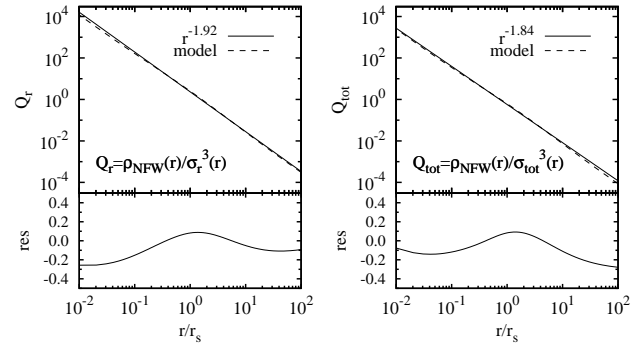


**Figure 12.** Radial profiles of  $\rho(r)/\sigma_r(r)^3$  (left panel) and  $\rho(r)/\sigma_{\text{tot}}(r)^3$  (right panel). The dashed lines show predictions of the model DF with the NFW density profile and parameters fitted to the median anisotropy profile shown in Fig. 4. The solid lines plot power-law functions with logarithmic slopes from Dehnen & McLaughlin (2005). In the lower panels we show relative residuals.

scribed e.g. by Mahdavi & Geller (2004). A more advanced and simulation-independent approach would be to treat the anisotropy profile as an unknown quantity, described by the three parameters introduced in our formulation. As a result one would obtain an estimate of the mass profile as well as anisotropy. Both methods require an additional study of the DF in projection and extensive tests on mock data sets. This will be the subject of our follow-up papers.

## ACKNOWLEDGMENTS

The simulations have been performed at the Altix of the LRZ Garching. RW and EL are grateful for the hospitality of Astrophysikalisches Institut Potsdam and Institut d’Astrophysique de Paris where part of this work was done. RW thanks A. Knebe for helpful advice and G. Boué for fruitful discussions. This work was partially supported by the Polish Ministry of Science and Higher Education under grant NN203025333 as well as by the Polish-German exchange program of Deutsche Forschungsgemeinschaft and the Polish-French collaboration program of LEA Astro-PF.

## REFERENCES

- An J. H., Evans N. W., 2006a, *AJ*, 131, 782
- An J. H., Evans N. W., 2006b, *ApJ*, 642, 752
- Ascasibar Y., Binney J., 2005, *MNRAS*, 356, 872
- Baes M., van Hese M., 2007, *A&A*, 471, 419
- Binney J., 1982, *MNRAS*, 200, 951
- Binney J., Tremaine S., 1987, *Galactic Dynamics*. Princeton Univ. Press, Princeton
- Cole S., Lacey C., 1996, *MNRAS*, 281, 716
- Colín P., Klypin A. A., Kravtsov A. V., 2000, *ApJ*, 539, 561
- Cuddeford P., 1991, *MNRAS*, 253, 414
- Cuddeford P., Louis P., 1995, *MNRAS*, 275, 1017
- Cuesta A. J., Prada F., Klypin A., Moles M., 2007, submitted to *MNRAS*, arXiv:0710.5520
- Dehnen W., McLaughlin D. E., 2005, *MNRAS*, 363, 1057
- Diemand J., Moore B., Stadel J., 2004, *MNRAS*, 352, 535
- Faltenbacher A., Diemand J., 2006, *MNRAS*, 369, 1698
- Fukushige T., Makino J., 2001, *ApJ*, 557, 533
- Gottlöber S., Yepes G., 2007, *ApJ*, 664, 117
- Hénon M., 1973, *A&A*, 24, 229

- Katgert P., Biviano A., Mazure A., 2004, *ApJ*, 600, 657  
Kazantzidis S., Magorrian J., Moore B., 2004, *ApJ*, 601, 37  
Klypin A., Gottlöber S., Kravtsov A. V., Khokhlov A. M., 1999, *ApJ*, 516, 530  
Kochanek C. S., 1996, *ApJ*, 457, 228  
Kravtsov A. V., Klypin A., Khokhlov A. M., 1997, *ApJS*, 111, 73  
Louis P. D., 1993, *MNRAS*, 261, 283  
Lokas E. L., 2002, *MNRAS*, 333, 697  
Lokas E. L., Hoffman Y., 2001, in Spooner N. J. C., Kudryavtsev V., eds, *Proc. 3rd International Workshop, The Identification of Dark Matter*. World Scientific, Singapore, p. 121  
Lokas E. L., Mamon G. A., 2001, *MNRAS*, 321, 155  
Lokas E. L., Mamon G. A., 2003, *MNRAS*, 343, 401  
Lokas E. L., Wojtak R., Gottlöber S., Mamon G. A., Prada F., 2006, *MNRAS*, 367, 1463  
Mahdavi A., Geller M. J., 2004, *ApJ*, 607, 202  
Mamon G. A., Lokas E. L., 2005, *MNRAS*, 363, 705  
Merritt D., 1985, *AJ*, 90, 1027  
Merritt D., Navarro J. F., Ludlow A., Jenkins A., 2005, *ApJ*, 624L, 85  
Natarajan P., Hjorth J., van Kampen E., 1997, *MNRAS*, 286, 329  
Navarro J. F., Frenk C. S., White S. D. M., 1997, *ApJ*, 490, 493  
Navarro J. F. et al., 2004, *MNRAS*, 349, 1039  
Osipkov L. P., 1979, *Soviet Astron. Lett.*, 5, 42  
Prada F., Klypin A. A., Simonneau E., Betancort-Rijo J., Patiri S., Gottlöber S., Sanchez-Conde M. A., 2006, *ApJ*, 645, 1001  
Saha P., 1992, *MNRAS*, 254, 132  
Spergel D. N. et al., 2007, *ApJS*, 170, 377  
Taylor J. E., Navarro J. F., 2001, *ApJ*, 563, 483  
van der Marel R. P., Magorrian J., Carlberg R. G., Yee H. K. C., Ellingson E., 2000, *AJ*, 119, 2038  
Voglis N., 1994, *MNRAS*, 267, 379  
Widrow L. M., 2000, *ApJS*, 131, 39  
Wilkinson M. I., Evans N. W., 1999, *MNRAS*, 310, 645  
Wojtak R., Lokas E. L., 2007, *MNRAS*, 377, 843  
Wojtak R., Lokas E. L., Gottlöber S., Mamon G. A., 2005, *MNRAS*, 361, L1  
Wojtak R., Lokas E. L., Mamon G. A., Gottlöber S., Prada F., Moles M., 2007, *A&A*, 466, 437

**APPENDIX A: THE VOLUME OF THE HYPERSURFACE**

The volume  $g(E, L)$  of the hypersurface  $S_{EL}(\mathbf{v}, \mathbf{r})$  of constant energy and angular momentum is defined by the integral

$$g(E, L)dEdL = \int_{S_{EL}(\mathbf{v}, \mathbf{r})} d^3v d^3r. \quad (\text{A1})$$

Introducing spherical coordinates and changing variables into  $E$ ,  $L$  and radius  $r$  one gets

$$g(E, L)dEdL = 8\pi^2 L dEdL \oint \frac{dr}{|v_r(E, L, r)|}, \quad (\text{A2})$$

where  $v_r$  is the radial velocity and the integral is equal to the radial period of the orbit. Using the radii of the pericentre  $r_p$  and the apocentre  $r_a$ , one can rewrite the final formula for  $g(E, L)$  in the following way

$$g(E, L) = 16\pi^2 L \int_{r_p}^{r_a} \frac{dr}{\sqrt{2\Psi(r) - 2E - L^2/r^2}}. \quad (\text{A3})$$

Integrating  $g(E, L)$  over the angular momentum we get the volume  $g_E(E)$  of the hypersurface of constant energy

$$g_E(E) = 16\pi^2 \int_0^{L_{\max}(E)} L dL \int_{r_p(L)}^{r_a(L)} \frac{dr}{\sqrt{2\Psi(r) - 2E - L^2/r^2}}. \quad (\text{A4})$$

Changing the order of the integrals and performing the integral over the angular momentum one obtains

$$g_E(E) = 16\pi^2 \int_0^{r_{\max}(E)} \sqrt{2(\Psi(r) - E)r^2} dr, \quad (\text{A5})$$

where  $r_{\max}(E)$  is the apocentre radius of the radial orbit ( $E = \Psi(r_{\max})$ ).

Considering a system of finite size  $V(\mathbf{v}, \mathbf{r})$  in phase space, one has to recalculate  $g(E, L)$  with the realistic hypersurface of constant  $E$  and  $L$  given by the Cartesian product  $S_{EL}(\mathbf{v}, \mathbf{r}) \times V(\mathbf{v}, \mathbf{r})$ . In particular, for a spherical system with a boundary in the form of a sphere of radius  $r_v$  the upper limit of the integral in (A3) and (A5) must be replaced by  $\min\{r_a, r_v\}$  and  $\min\{r_a, r_{\max}(E)\}$  respectively.

**APPENDIX B: THE ENERGY PART OF THE DISTRIBUTION FUNCTION**

The energy part of the DF  $f_E(E)$  introduced in section 4 is related to the density profile by

$$\rho(r) = \iiint f_E(E) \left(1 + \frac{L^2}{2L_0^2}\right)^{-\beta_\infty + \beta_0} L^{-2\beta_0} d^3v. \quad (\text{B1})$$

Although the main part of this paper concerns the DF consistent with the NFW profile, we keep within the appendix a general density  $\rho(r)$  so that the final formulae of inversion could be applied to any potential-density pair.

Changing variables in the integral (B1) into the energy and angular momentum one gets

$$\rho(r) = 2^{3/2 - \beta_0} \pi r^{-1} L_0^{1 - 2\beta_0} \int_0^\Psi f_E(E) dE \int_0^x \frac{(1 + \lambda)^{-\beta_\infty + \beta_0} \lambda^{-\beta_0}}{\sqrt{x - \lambda}} d\lambda, \quad (\text{B2})$$

where  $x = r^2(\Psi - E)/L_0^2$  and  $\lambda = L^2/(2L_0^2)$ . The integral over the  $\lambda$  variable is evaluated analytically so that (B2) can be rewritten in the form

$$\rho(r)r^{2\beta_0} = (2\pi)^{3/2} 2^{-\beta_0} \frac{\Gamma(1 - \beta_0)}{\Gamma(3/2 - \beta_0)} \int_0^\Psi f_E(E) (\Psi - E)^{1/2 - \beta_0} K(\Psi, E) dE \quad (\text{B3})$$

with a kernel of the integral given by

$$K(\Psi, E) = (1 + x)^{-\beta_\infty + \beta_0} {}_2F_1(1/2, \beta_\infty - \beta_0, 3/2 - \beta_0, x/(1 + x)), \quad (\text{B4})$$

where  ${}_2F_1$  stands for the hypergeometric function. Equation (B3) is a Volterra integral of the first kind. In the general case of models with varying anisotropy, when  $\beta_\infty \neq \beta_0$  and  $L_0 < \infty$ , it has no analytical solution for  $f_E(E)$  due to the complexity of expression (B4). However, as shown by Cuddeford & Louis (1995), this kind of integral can be quite easily inverted numerically. Below we adapt their method to our problem.

For  $E \rightarrow 0$  and  $\Psi \gg E$  the integral kernel can encounter a singularity, i.e.  $K(\Psi, E) \propto E^{\beta_\infty - \beta_0}$ . In order to avoid this behaviour, we define a smooth integral kernel  $\hat{K}(\Psi, E)$  which is free of such a feature

$$\hat{K}(\Psi, E) = E^{-\beta_\infty + \beta_0} K(\Psi, E). \quad (\text{B5})$$

By analogy we introduce a smooth energy part of the DF which is a regular function for energy approaching 0

$$\hat{f}_E(E) = E^{3/2 - \nu} f_E(E). \quad (\text{B6})$$

The value of  $\nu$  is determined from the limit of  $\rho(r)$  at small potential ( $\Psi \ll 1$  and  $r \rightarrow \infty$ ) in equation (B3), for which

$$\rho(r)r^{2\beta_0} \propto \Psi(r)^{\nu-\beta_0} r^{2(-\beta_\infty+\beta_0)}, \quad (\text{B7})$$

which immediately gives  $\nu$  in terms of  $\beta_0$ ,  $\beta_\infty$  and the asymptotic slopes of the potential and density. In particular, for the NFW density profile one gets  $\nu = 3 - 2\beta_\infty + \beta_0$ .

Using formulae (B5) and (B6) we can rewrite equation (B3) in the following form

$$\hat{\rho}(r) = C_{\beta_0} \int_0^\Psi \hat{f}_E(E) \hat{K}(\Psi, E) (\Psi - E)^{1/2-\beta_0} E^{\nu-3/2+\beta_\infty-\beta_0} dE, \quad (\text{B8})$$

where  $\hat{\rho} = \rho(r)r^{2\beta_0}$  and  $C_{\beta_0}$  stands for all coefficients in front of the integral (B3). Following Cuddeford & Louis (1995) we introduce discrete vectors of the potential  $\Psi_j = j\epsilon$ , radius  $r_j = r(\Psi_j)$  and density  $\hat{\rho}_j = \rho(r_j)r_j^{2\beta_0}$ , where  $j$  is an integer number and  $\epsilon = 1/j \ll 1$ . For any  $\hat{\rho}_j$  we can split the integral (B8) into a sum

$$\hat{\rho}_j = C_{\beta_0} \sum_{i=1}^{i=j} \int_{(i-1)\epsilon}^{i\epsilon} \hat{f}_E(E) \hat{K}(j\epsilon, E) (j\epsilon - E)^{1/2-\beta_0} E^{\nu-3/2+\beta_\infty-\beta_0} dE. \quad (\text{B9})$$

In order to apply any numerical algorithm to invert equation (B9) with respect to  $\hat{f}_E(E)$ , one has to assume that  $\epsilon$  is sufficiently small so that the variations of  $\hat{f}_E(E)$  and  $\hat{K}(j\epsilon, E)$  within subsequent integration ranges are negligible. Then one can approximate both functions by their values at  $(i - 1/2)\epsilon$ , i.e. the middle points of the energy range. This approach was used by Cuddeford & Louis (1995) and favoured over other methods involving higher order interpolation (see e.g. Saha 1992). Applying this approximation to equation (B9) we get

$$\hat{\rho}_j = C_{\beta_0} \sum_{i=1}^{i=j} \hat{f}_{E_i} \hat{K}(j\epsilon, (i - 1/2)\epsilon) I_{ij} \quad (\text{B10})$$

with  $\hat{f}_{E_i} = \hat{f}_E((i - 1/2)\epsilon)$  and the matrix  $I_{ij}$  defined in the following way

$$\begin{aligned} I_{ij} &= \int_{(i-1)\epsilon}^{i\epsilon} E^{\nu-3/2+\beta_\infty-\beta_0} (j\epsilon - E)^{1/2-\beta_0} dE \\ I_{ij} &= (j\epsilon)^{\nu+\beta_\infty-2\beta_0} [B_{i/j}(\nu + \beta_\infty - \beta_0 - 1/2, 3/2 - \beta_0) - B_{(i-1)/j}(\nu + \beta_\infty - \beta_0 - 1/2, 3/2 - \beta_0)], \end{aligned} \quad (\text{B11})$$

where  $B_z(x, y)$  is the incomplete beta function. As shown by Cuddeford & Louis (1995), the solution of (B10) for  $\hat{f}_{E_i}$  can be obtained by evaluating iteratively the following expression

$$\hat{f}_{E_j} = \frac{\hat{\rho}_j / C_{\beta_0} - \sum_{i=1}^{i=j-1} \hat{K}(j\epsilon, (i - 1/2)\epsilon) I_{ij} \hat{f}_{E_i}}{\hat{K}(j\epsilon, (j - 1/2)\epsilon) I_{jj}} \quad (\text{B12})$$

with the initial value  $\hat{f}_{E_1}$  given by

$$\hat{f}_{E_1} = \frac{\hat{\rho}_1 / C_{\beta_0}}{\hat{K}(\epsilon, \epsilon/2) I_{11}}. \quad (\text{B13})$$

### APPENDIX C: VELOCITY MOMENTS

All non-vanishing moments of the radial or tangential velocity at a given radius  $r$  are defined by the integral

$$\langle v_i^{2n} \rangle(r) = \frac{1}{\rho(r)} \iiint f_E(E) \left(1 + \frac{L^2}{2L_0^2}\right)^{-\beta_\infty+\beta_0} L^{-2\beta_0} v_i^{2n} d^3v, \quad (\text{C1})$$

where  $i$  is a subscript indicating the velocity component in spherical coordinates and  $n$  is an integer number. By analogy with steps (B2) and (B3) from Appendix B, one can evaluate the angular momentum part of the integral and simplify the expression to the following form

$$\langle v_i^{2n} \rangle(r) = \frac{2^{3/2+n-\beta_0} \pi}{r^{2\beta_0} \rho(r)} \int_0^\Psi f_E(E) (\Psi - E)^{1/2+n-\beta_0} K_i(\Psi, E) dE, \quad (\text{C2})$$

where the kernel functions for the radial ( $i = r$ ) and tangential ( $i = \theta = \phi$ ) component of the velocity field are given respectively by

$$K_r(\Psi, E) = \frac{\Gamma(3/2 + n)\Gamma(1 - \beta_0)}{(1/2 + n)\Gamma(3/2 + n - \beta_0)} (1 + x)^{-\beta_\infty+\beta_0} {}_2F_1(1/2 + n, \beta_\infty - \beta_0, 3/2 + n - \beta_0, x/(1 + x)) \quad (\text{C3})$$

$$K_\theta(\Psi, E) = \frac{\Gamma(1/2 + n)\Gamma(1 + n - \beta_0)}{\Gamma(1 + n)\Gamma(3/2 + n - \beta_0)} (1 + x)^{-\beta_\infty+\beta_0} {}_2F_1(1/2, \beta_\infty - \beta_0, 3/2 + n - \beta_0, x/(1 + x)). \quad (\text{C4})$$

Once  $f_E(E)$  is calculated in terms of the  $f_{E_i}$  vector it is easy to evaluate numerically the integral (C2) and obtain the profile of any velocity moment.

An interesting property of the model is the ratio of any non-vanishing moment of the tangential velocity to the corresponding moment of the radial velocity in the limit of small and large radii. Introducing spherical coordinates in (C1) and performing the integral with two asymptotes of  $f_L(L)$  given by (22), one can show that this ratio is the following function of  $\beta_0$  or  $\beta_\infty$

$$\frac{\langle v_\theta^{2n} \rangle}{\langle v_r^{2n} \rangle} = \begin{cases} \frac{\Gamma(1+n-\beta_0)}{\Gamma(1-\beta_0)\Gamma(1+n)} & \text{for } r \rightarrow 0 \\ \frac{\Gamma(1+n-\beta_\infty)}{\Gamma(1-\beta_\infty)\Gamma(1+n)} & \text{for } r \rightarrow \infty. \end{cases} \quad (\text{C5})$$